Characterization of the NASA Langley Arc Heated Scramjet Test Facility using NO PLIF

F. Gray Kidd III,[*] Venkateswaran Narayanaswamy[†]
North Carolina State University, Raleigh, NC, 27695

Paul M. Danehy,[‡] Jennifer A. Inman,[§] Brett F. Bathel[**]
Advanced Sensing and Optical Measurement Branch
NASA Langley Research Center, MS 493, Hampton, VA, 23681-2199

Karen F. Cabell,[††] Neal E. Hass,[‡‡] Diego P. Capriotti,[§§] Tomasz G. Drozda[***]
Hypersonic Airbreathing Propulsion Branch
NASA Langley Research Center, MS 168, Hampton, VA, 23681-2199

and

Craig T. Johansen[†††]
University of Calgary, Calgary, AB, T2N 1N4

The nitric oxide planar laser-induced fluorescence (NO PLIF) imaging was used to characterize the air flow of the NASA Langley Arc Heated Scramjet Test Facility (AHSTF) configured with a Mach 6 nozzle. The arc raises the enthalpy of the test gas in AHSTF, producing nitric oxide. Nitric oxide persists as the temperature drops through the nozzle into the test section. NO PLIF was used to qualitatively visualize the flowfield at different experimental conditions, measure the temperature of the gas flow exiting the facility nozzle, and visualize the wave structure downstream of the nozzle at different operating conditions. Uniformity and repeatability of the nozzle flow were assessed. Expansion and compression waves on the free-jet shear layer as the nozzle flow expands into the test section were visualized. The main purpose of these experiments was to assess the uniformity of the NO in the freestream gas for planned experiments, in which NO PLIF will be used for qualitative fuel-mole-fraction sensitive imaging. The shot-to-shot fluctuations in the PLIF signal, caused by variations in the overall laser intensity as well as NO concentration and temperature variations in the flow was 20-25% of the mean signal, as determined by taking the standard deviation of a set of images obtained at constant conditions and dividing by the mean. The fluctuations *within* individual images, caused by laser sheet spatial variations as well as NO concentration and temperature variations in the flow, were about 28% of the mean in images, determined by taking standard deviation within individual images, dividing by the mean in the same image and averaged over the set of images. Applying an averaged laser sheet intensity correction reduced the within-image intensity fluctuations to about 10% suggesting that the NO concentration is uniform to within 10%. There was no significant difference in flow uniformity between the low and high enthalpy settings. While not strictly quantitative, the temperature maps show qualitative agreement with the computations of the flow.

---

[*] Graduate Student, Department of Mechanical Engineering, AIAA Member.
[†] Assistant Professor, Department of Mechanical Engineering, AIAA Member.
[‡] Research Scientist, AIAA Associate Fellow.
[§] Research Scientist, AIAA Member.
[**] Research Scientist, AIAA Member.
[††] Research Scientist, AIAA Member.
[‡‡] Research Engineer, AIAA Senior Member.
[§§] Research Engineer.
[***] Research Aerospace Engineer, AIAA Senior Member.
[†††] Assistant Professor, Department of Mechanical and Manufacturing Engineering, AIAA Senior Member.

I. Introduction

ARC-heated facilities are important hypersonic ground test facilities that are capable of producing high-enthalpy environments similar to those experienced during hypersonic vehicle flight and reentry. These facilities are used for several applications like testing heat shields used in hypersonic vehicles, testing scramjet engines,[1] understanding boundary layer transition, as well as providing data for the validation of computational models used in hypersonic applications. Many of the early measurements in hypersonic facilities used intrusive probes that provided pointwise measurements of flow properties. These techniques had the advantage of being relatively robust and simple to implement but often at the expense of perturbing the flow. Developments in laser-based imaging technologies allowed for measurements that were less invasive and in some cases, capable of providing multi-dimensional and multi-variable measurements of flow properties, albeit often at the expense of complexity.

Planar laser-induced fluorescence (PLIF), since its conception over 25 years ago has proved to be a versatile non-intrusive diagnostic tool capable of making quantitative measurements. PLIF uses the excitation of atoms, molecules or radicals such as nitric oxide (NO),[2] hydroxyl (OH),[3] iodine,[4] krypton,[5,6] etc. present in the flow (or seeded externally) to measure the flow properties. NO is a commonly probed molecule, among other reasons, because it occurs naturally in many hypersonic facilities such as shock tunnels and arc-heated facilities at NASA Langley and is well understood spectroscopically. NO PLIF has been demonstrated by previous researchers for thermometry, velocimetry and flow visualization applications. Koch et al.[7] scanned several transitions of NO in their high-enthalpy facility to compute the mean rotational and vibrational temperature. Their vibrational temperature measurements were validated by accompanying coherent anti-Stokes Raman scattering (CARS) measurements.[8] While the scanning technique provides accurate temperature measurements, it requires long tunnel run times. In a subsequent work, Palma[3] implemented an integrated two- and multi-line fluorescence ratiometric technique to obtain the temperature field in a Mach 7.7 shock tunnel that has very short run-times, on the order of a few milliseconds, which precludes spectral scans using existing technology. Using this technique, Palma achieved a rotational temperature uncertainty of less than 4%. A similar strategy was also used by Palma et al.[9] to make boundary layer temperature measurements.

NO PLIF has also been used as a visualization tool in hypersonic flowfields. Fox et al.[10] have used NO PLIF to visualize the flow over a blunt fin attached to a flat plate, which mimics the wing/body junction of hypersonic vehicles. Using NO PLIF, it was shown that the run time in the T3 free piston shock tunnel at the Australian National University is sufficient for flow establishment and the separated flow in front of the fin was accurately measured. More recently, Ivey et al.[11] visualized the reaction control system (RCS) jets of the Orion crew exploration vehicle reentry in NASA's 31-inch Mach 10 wind tunnel using 2D NO PLIF imaging. Agreement was obtained between CFD simulations and the mean trajectory and velocity profiles of two different RCS yaw jets. This technique was extended to three-dimensional reconstruction of the evolution of the RCS jet by Inman et al.[12] The visualization enabled insights into spatially and temporally resolved mean evolution of the RCS jets and the location and characteristics of instantaneous turbulent structures (from 2D slices).

The Arc-Heated Scramjet Test Facility (AHSTF) at NASA Langley is to be used for mixing tests to develop improved fuel-air mixing strategies applicable to high Mach number scramjet flights. The tests will use NO PLIF for qualitative or semi-quantitative flow visualization of the fuel-air mixing process.[13] However, at the reduced enthalpy conditions planned for upcoming mixing studies, it was unclear whether there would be sufficient NO present in the flow to serve as the marker for fuel-air mixing visualization. Therefore, the existence and uniformity of NO needed to be assessed at the planned mixing test conditions. Furthermore, the mixing tests will require longer than normal operating times (5 minutes compared to the normal 15 to 30 seconds used previously in the AHSTF). Consequently, the test section pressure will increase above normal levels, resulting in wave structures at the nozzle exit which may impact the fuel-air mixing experiment. The facility will also need to vary operating arc currents while maintaining constant enthalpy to extend electrode life during long runs. The influence of the changes in the arc current on the temperature and NO PLIF signals is determined in this study. Additionally, we evaluated the ability of NO PLIF to make NO temperature measurements in the facility, which would be useful in future fuel-air mixing and scramjet engine tests in AHSTF.

II. Experiment

A. Arc heated Scramjet Test Facility

The AHSTF has been used as a hypersonic air-breathing propulsion test facility since 1976. The facility uses arc-heated air to duplicate true flight stagnation enthalpy conditions, typically for a flight Mach number range of 4.7 to 8.[1,14,15] To generate the necessary high enthalpy flow, a portion of the incoming

air is heated by an electric arc to a bulk temperature of approximately 4000 K and as a result, nitric oxide is formed.[16,17,18] Figure 1 shows a schematic of the facility. There are three primary facility components upstream of the test section: the arc heater, the plenum and the nozzle. The arc heater is a cylindrical vessel comprised of an upstream and downstream electrode. The air entering the heater, referred to as *main air*, is heated by an electric arc that is established between the upstream and downstream electrodes. Except for the arc attachment regions, the arc is mainly confined to the centerline of the heater by the vortex flow resulting from the swirl injection of the main air. According to Ref. 19, in a typical arc heater, about 5 percent of the total air is heated directly by the arc and becomes fully dissociated; the remainder of the air is heated relatively slowly by radiation and conduction and is dissociated to a lesser degree.

The heated main air enters the plenum where unheated air is injected radially to break up the swirling motion of the main air exiting the heater and to enhance mixing of the two air streams. The ambient temperature *bypass air* is added in an amount necessary to achieve a mixture stagnation enthalpy corresponding to the desired altitude and flight Mach number simulation. This method of heating only a portion of the total air to elevated temperatures and then mixing it with cooler air to achieve the desired test conditions is necessary because the heater cannot operate in a stable mode while processing the full facility air flow rates. The resulting air mixture exiting the plenum is expanded through a converging/diverging supersonic nozzle and enters the four foot diameter test section. For the present tests, the "Mach 6 2D" nozzle was used. This nozzle has a 10 in. by 10 in. (25.4 cm x 25.4 cm) nozzle exit area. The nominal plenum stagnation conditions for the present tests were a stagnation pressure of 625 psia (4.31 MPa) and stagnation enthalpies ranging from 0.78 to 1.02 MJ/kg. The nozzle exit Mach number is approximately 6.4. Note that the enthalpy used is much lower than that required to simulate the true enthalpy in a Mach 6 or greater flight. Such low enthalpies (low temperatures) were chosen to increase the Reynolds number to match the high Reynolds number expected for high Mach number flight to be simulated in the planned mixing experiments. In past work in this facility, which occurred at higher enthalpies, the mole fraction of NO was computed to "freeze" at the nozzle throat, resulting in roughly 1-3% NO in the freestream flow.[18,18] In addition to this chemical nonequilibrium, recent computations[19] (not reported here) also indicated that the flow is in a state of vibrational non-equilibrium. Going into this work it was unclear from computations whether NO would be present in the freestream at these conditions.

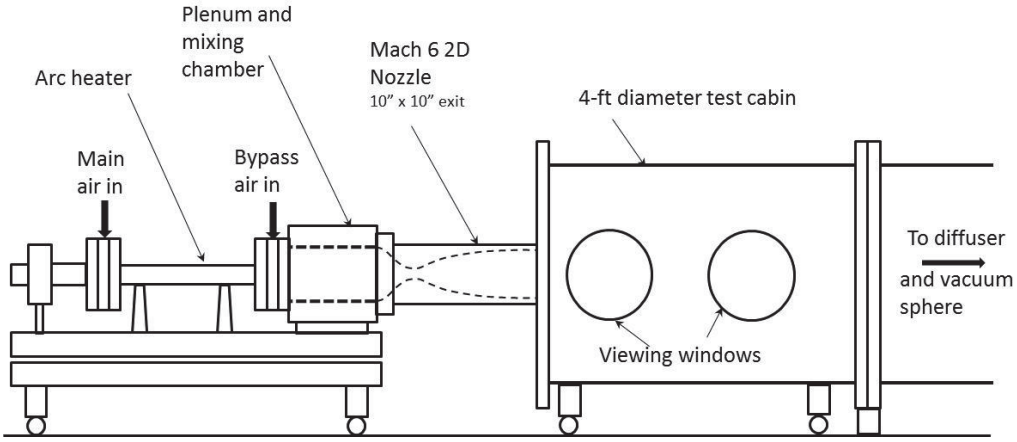

Figure 1. Facility Schematic. Flow passes left to right from the heater, through the Mach 6 nozzle and into the test cabin.

B. The NO PLIF Method

Nitric oxide is generated as one of the products of the high-current thermal arc generated in the arc heater. The generated NO persists during the relatively short flow residence time between the stagnation chamber and the measurement location. The NO acts as in-situ flow tracer that can be imaged using planar laser-induced fluorescence (PLIF). NO PLIF uses an ultraviolet laser sheet to interrogate a slice in the flow containing NO. This UV light excites fluorescence from the NO molecules, which is detected by a digital camera. Details of the measurement system used in this experiment, as well as the experimental procedure used, can be found in Refs. 14 and 15.

One of NASA's two mobile PLIF systems was installed next to the AHSTF facility as shown in Fig. 2. The laser system uses a Spectra Physics Pro-230 Nd:YAG laser to pump a Sirah Cobra Stretch dye laser and Sirah Frequency Conversion Unit (FCU). The dye laser was operated near 624 nm and was sum-frequency mixed with the third harmonic of the Nd:YAG laser to produce the UV light used to excite NO. The resulting tunable laser output, near

226 nm, was tuned to excite a variety of strongly fluorescing spectral lines of NO. The UV laser beam passed through windows mounted into an aluminum blank manufactured to replace the facility window. The laser beam was formed into a laser sheet using a pair of lenses (usually a cylindrical lens followed by a spherical lens). Table 1 describes the different configurations used to form the laser sheet as well as the different camera lenses used to measure the fluorescence. The same cameras, excitation schemes, etc., were used as in past work, including high-efficiency filters (Layertec GmbH, Germany, <1% transmission at 226 nm and >80% transmission at 235-280 nm) that were used to transmit the LIF signal while rejecting the laser scatter. Additionally, a 2-mm thick UG-5 filter was used to reject flow luminosity, much of which was in the visible spectrum. The fluorescence was imaged onto a gated, intensified CCD (Princeton Instruments PIMAX-II) using the lenses listed in Table 1. The camera magnifications were measured from images acquired of a regular pattern of dots of known spacing (known as a *dotcard*), with this dotcard placed in the image plane, as shown in Figure 4. The images were obtained at a rate of 10 Hz with flow-stopping time resolution (<1 microsecond). The final images were corrected for the background signal levels and corrected for perspective and lens distortions. The spatial distribution of intensity in the laser sheet was not monitored.

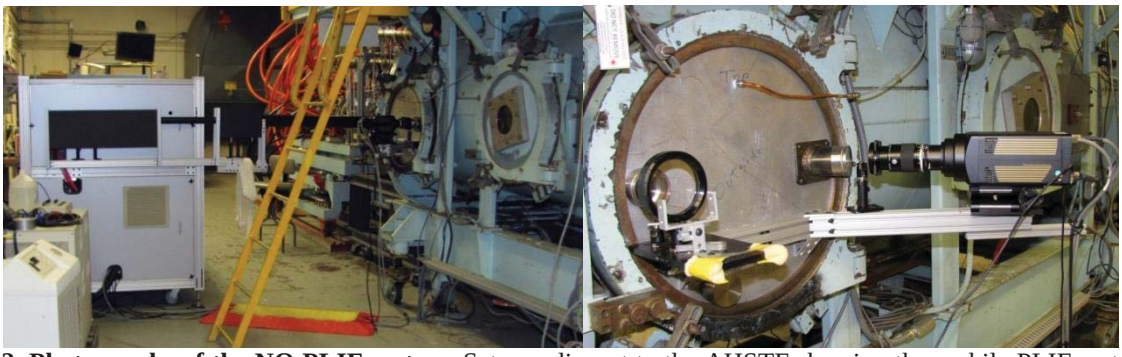

Figure 2. Photographs of the NO PLIF system. Set up adjacent to the AHSTF showing the mobile PLIF cart and facility (left) and detail of camera setup (right). The configuration shown was used in the first set of experiments (Configuration 1 in Table 1).

Table 1. Laser Sheet Configurations

Configuration	Run(s)	Laser Sheet Orientation	Laser Sheet Direction	Laser Sheet Divergence	Camera Lens focal length
1	502-519	Vertical	Spanwise	Collimated	105 mm
2	520-527	Vertical	Spanwise	Diverging	45 mm
3	528	Horizontal	Spanwise	Diverging	45 mm
4	529-532	Horizontal	Spanwise and Angled	Collimated	105 mm

C. Measurement configurations

A total of four laser configurations were used in this experiment. Two were done with a vertical laser sheet orientation parallel to the nozzle exit plane. These allowed for temperature maps to be compared with CFD predictions. These laser configurations were used for temperature determination studies. The other two configurations, used mainly for flow visualization, were done in a plane perpendicular to the nozzle exit plane to allow for flow visualization mapping of wave features caused by the rising pressure of the test section.

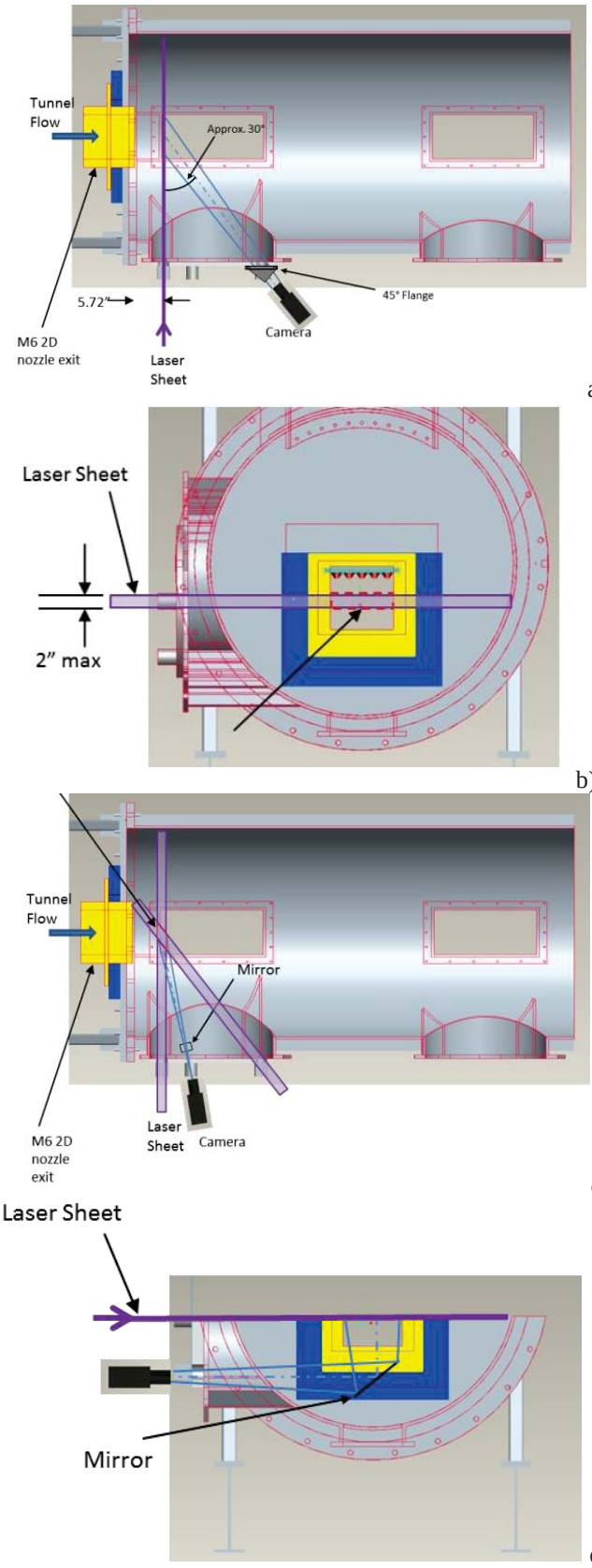

Figure 3. Laser configuration of AHSTF test section. Collimated configurations are shown; however the beam could be diverged to cover a larger area. (a,b) Top and End views of Configuration 1; (c,d) Top and End views of Configuration 4. For end views, flow direction is out-of-page.

D. Numerical simulation

The numerical simulations were performed using version 6.2.0 of the Viscous Upwind aLgorithm for Complex flow ANalysis (VULCAN)[20] CFD code. VULCAN is a multi-block; structured-grid, cell-centered, finite-volume solver widely used for all-speed flow simulations. For this work, the Reynolds-averaged Navier- Stokes (RANS) equations were solved. The advective terms were computed using a MUSCL scheme[21] with the Low-Dissipation Flux-Split Scheme (LDFSS) of Edwards.[22] A non-reacting, thermally perfect mixture of 21% oxygen (O_2), 78% nitrogen (N_2), and 1% nitrogen oxide (NO) was considered. A small amount of NO was added to account for production of this species in the arc-heater of the experimental facility. The thermodynamic properties of mixture components were computed using curve fits of McBride et al.[23] The governing equations were integrated using an implicit diagonalized approximate factorization (DAF) [24]method.

The current work used the baseline blended k-ω/k-E turbulent physics model of Menter.[25] The Reynolds heat and species mass fluxes were modeled using a gradient diffusion model with turbulent Prandtl and Schmidt numbers of 0.9 and 0.5, respectively. Wilcox wall matching functions[26] were also used to reduce the near-wall grid resolution requirements. Further taking advantage of the nozzle symmetries, only a quarter of the full nozzle geometry was simulated. This quarter-geometry grid consisted of about 3.9 million cells. Subsonic inflow boundary conditions, specifying a total pressure of 625 psi (4.31 MPa) and temperature of 1732 R (962 K) were used at the inflow located upstream of the nozzle throat for the high enthalpy case. For low enthalpy a total pressure of 625 psi (4.31 MPa) and temperature of 1301 R (728 K) were used. First-order extrapolation was used at the supersonic outflow of the nozzle. The walls were modeled using a no-slip boundary condition for the velocities. The y^+ values ranged from about 10 to 80, with the average of about 25 and the largest values located upstream and at the nozzle throat. The temperatures at the nozzle walls were obtained by locally solving a one-dimensional heat conduction equation with the experimentally obtained nozzle outer wall temperatures as an input. The flow was initialized using a solution of the one-dimensional isentropic and adiabatic converging-diverging nozzle problem.

The simulations converged by about four orders of magnitude, at which point residuals became constant. Simultaneously, the total integrated mass flow at the nozzle exit and the total integrated heat flux on the walls remained constant as well. A grid sensitivity study was performed with negligible changes in flow properties being computed when the grid density was changed by a factor of two. Exit conditions from both simulations are given below in Table 2.

Table 2. Reservoir and freestream conditions for nozzle centerline based on CFD.

Enthalpy	Stagnation Pressure	Stagnation Temperature	Freestream Static Pressure	Freestream Static Temperature
Low	4.32 MPa (626 psi)	1301 R (728 K)	1.77 kPa (0.257 psi)	81 K (146 R)
High	4.32 MPa (626 psi)	1732 R (962 K)	1.81 Pa (0.263 psi)	110 K (198 R)

III. Results

The overall objective of this work is the assessment of NO content/uniformity/suitability to use as tracer for upcoming mixing tests. To achieve this objective we employed NO PLIF technique to quantify the uniformity of the NO in the flow. Also of interest was to assess the temperature uniformity of the AHSTF and delineate the flow features during different tunnel operating conditions. In anticipation for planned fuel-air mixing studies, it is necessary to establish that we obtain adequate NO PLIF signals at all run conditions. Further, we qualitatively investigate the extraneous effects like inherent non-uniformity of NO due to inhomogeneous arc-heating and spatial non-uniformity due to laser-sheet inhomogeneity. Subsequently, we quantify the uncertainty in temperature caused by these extraneous effects.

A. NO PLIF signal levels at different enthalpy settings

The experimental program was conducted at two stagnation enthalpy settings—335 Btu/lbm (0.78 MJ/kg) and 450 Btu/lbm (1.05 MJ/kg)—and three (sometimes varying) arc current settings. A representative single-shot image corresponding to the $A^2\Sigma^+ \leftarrow X^2\Pi$ transition $R_2(12)$ line for the two enthalpy settings are shown in Fig. 4(a,b) along with the ensemble average of 100 NO PLIF images for both settings in Fig. 4(c,d). The contrast levels have been adjusted to allow direct comparison of the images. In Figure 4, the laser sheet is directed from left to right. Horizontal streaks in image are caused by variations in laser sheet. Variation in brightness left to right is caused by attenuation of the laser sheet because of absorption by the NO in the flow. Structures at the edges of the "core" flow are shear-layer instabilities, probably containing variations in NO concentration and temperature (which result in varying PLIF signal intensity) due to mixing with the surrounding stagnant fluid. The most significant finding is that

there is strong NO PLIF signal intensity (thousands of counts), with sufficient signal to noise ratio to provide visualizations of fuel-air mixing experiment, though the uniformity of the signal will be assessed below.

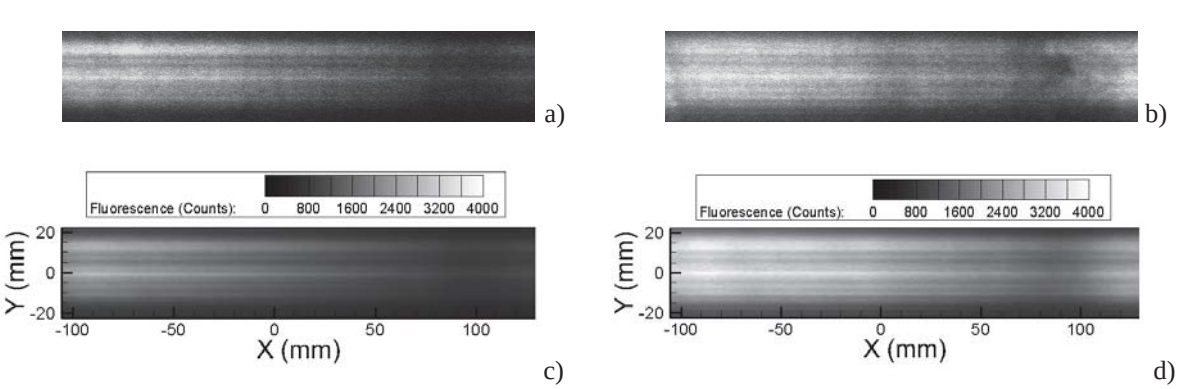

Figure 4. Comparison of low-enthalpy and high-enthalpy settings. Flow is out of the page and laser direction is from left to right. The core flow spans from -100 mm to 100 mm with the turbulent shear layer showing at the left and especially the right side(s). Images (a,b) show single-shot images while (c,d) show averaged fluorescence images.

The signal increase between the two enthalpy settings is roughly 25%. From our simulations using NO PLIF code (LINUS[25]) we observe that quantitative increase in $R_2(12)$ signals due to increase in static temperature between the two enthalpy settings (see Section 5) is less than 5%. Hence, the increase in NO PLIF signal with enthalpy is attributable to a greater percentage of generated NO at the higher-enthalpy setting.

We further studied the influence on time-varying changes in stagnation enthalpy on the NO PLIF signals to establish the existence of a monotonic response of the NO PLIF to stagnation enthalpy. During the experimental run, the stagnation enthalpy was continuously increased from 280 Btu/lbm (0.651 MJ/kg) through 500 Btu/lbm (1.16 MJ/kg) and was subsequently decreased back to 280 Btu/lbm. Further, the $Q_1(5)$ NO rotational line was used, which exhibited a similar qualitative response to temperature as the $R_2(12)$ line for the range of static temperatures obtained. This stronger Q-branch transition was chosen to be more strongly absorbing to potentially allow NO concentration measurements to be obtained from the decay in incident laser intensity (the results of these concentration measurements are not reported here). The laser energy and the optics are almost identical to those of Fig. 4. Figure 5 shows the background-subtracted NO PLIF signals as the enthalpy of the flow was varied continuously during an experimental run. The plotted NO PLIF signals represent a spatial average across the core flow. The lowest NO PLIF signal occurs at the lowest enthalpy setting of 280 Btu/lbm. The average NO PLIF signal monotonically increases with enthalpy from about 3000 to 15000 counts as the enthalpy increases to 500 Btu/lbm (1.16 MJ/kg), a 300% increase in signal over this range. Between 330 Btu/lbm (0.768 MJ/kg) and 450 Btu/lbm (1.05 MJ/kg), the signal changes from about 5000 counts to 13000 counts, which is a greater fractional change than that of Fig. 4. The differences in the fractional increase in signals with enthalpy between Fig. 4 and Fig. 5 may be attributed in part to the difference in transitions chosen. From our simulation using LINUS, we observed that the $Q_1(5)$ transition exhibits a higher increase in signal intensity with temperature compared to the $R_2(12)$ transition for the static temperature range of this test. About 50% (of the 300%) signal increase shown in Fig. 5 can be attributed to

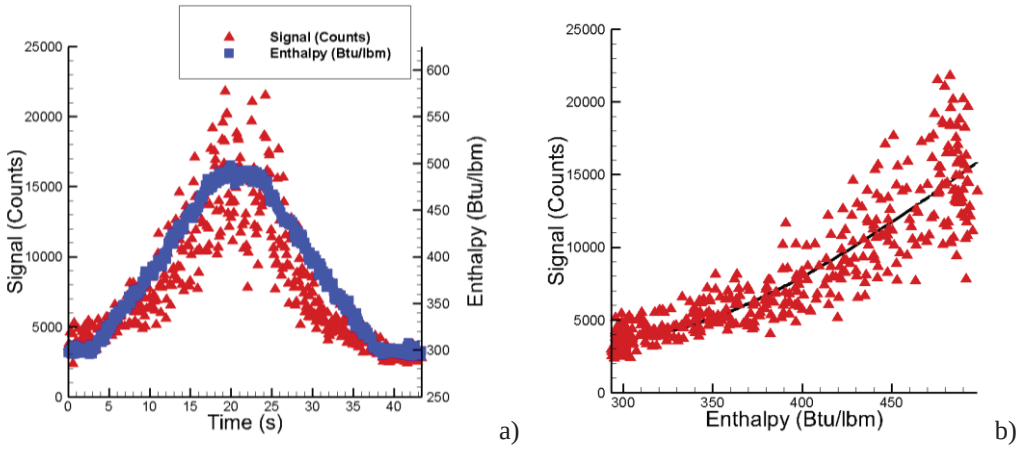

Figure 5. Correlation of NO fluorescence signal with flow enthalpy. The $Q_1(5)$ line was probed.

the increase in the population of the rotational level probed. Finally, we note that the NO PLIF signal at the end of the run is smaller than that at the beginning of the run by about 10% at the same enthalpy setting. This is mainly because of the gradual and continuous drop in the laser energy during the run time. Future tests would benefit from recording the laser energy on a single-shot basis and correcting the data for variations in laser energy.

B. Effect of Arc Current on NO PLIF Signal

The longer run times of AHSTF needed by future fuel-air mixing experiments will require variation of the arc current during a run to extend electrode life. The variation in arc current may potentially change the amount of NO generated, or the flow temperature, which may lead to additional uncertainty in the data reduction procedures. Thus, understanding the effect of changing arc current on the NO PLIF signal is critical for future experimental campaigns. Figure 6 shows the variation of NO PLIF signal count during an experimental run where the arc-current was periodically varied. It can be observed that the NO PLIF signals do not exhibit corresponding periodicity. Further, the NO PLIF signals remain approximately constant during the first 20 seconds of the run while the arc current is ramped up to its peak value. This is followed by a monotonic decay of NO PLIF signal, which again has no correlation with the arc current time-series (and which we attribute to a monotonic decrease in laser energy over the course of the run). Thus, we conclude that the NO PLIF signal intensity is independent of the arc current of the facility for a fixed enthalpy and does not interfere with data reduction.

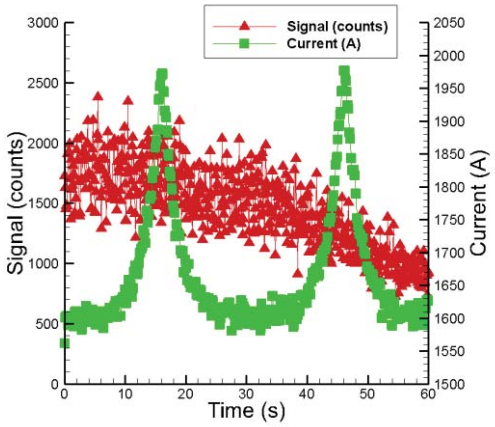

Figure 6. Fluorescence at varied current but constant enthalpy.

C. Spatial uniformity of NO PLIF signals

Having established that adequate NO PLIF signals are present to provide visualizations (see Figure 4) in upcoming fuel-air mixing experiments, the uniformity of the NO PLIF field was assessed. The causes for non-uniformity include the inherent spatial inhomogeneity in the NO during its production and transport, the unsteady turbulent shear layer, and the shot-to-shot changes in laser sheet profile. Figure 7 shows the standard deviation (value of NO PLIF intensity at each pixel), normalized by the corresponding ensemble-average intensity, for 100 images, which shows how much the PLIF intensity varies shot-to-shot in the experiment. Figure 7(a) corresponds to the low enthalpy setting (335 Btu/lbm, 0.779 MJ/kg) and Fig. 7(b) corresponds to the high enthalpy setting (440 Btu/lbm, 1.02 MJ/kg). The typical value ranges between 18 - 25% in the core flow at the low enthalpy setting. The high-enthalpy setting shows a region of similarly low fluctuations that correspond to the nozzle core flow, but also shows larger fluctuations in the regions corresponding to the turbulent shear layer. In particular, the mean-normalized standard-deviation at for high enthalpy settings is within 20% in the nozzle core flow. The fluctuations within images due to laser sheet inhomogeneity, temperature and NO concentration variations was also assessed. The standard deviation for the core flow of each image was calculated and then normalized by its intensity. The average fluctuation was 27% of the mean for the low enthalpy setting and

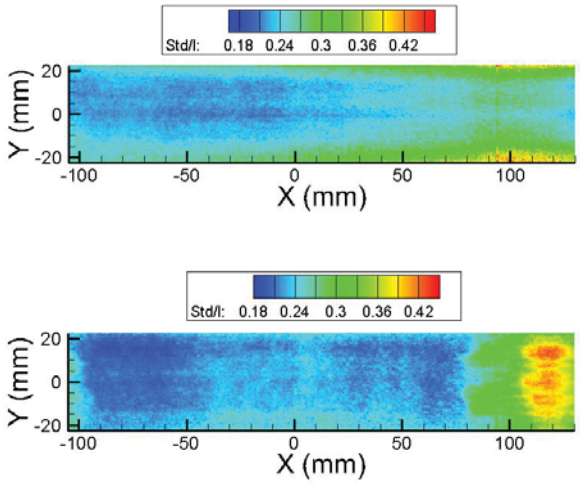

Figure 7. Fluctuations of PLIF intensity, normalized by mean intensity, for 100 images. Fig. 7(a) shows the low enthalpy 335 Btu/lbm (0.779 MJ/kg) case while 7(b) shows the high enthalpy 440 Btu/lbm (1.02 MJ/kg) case.

only slightly larger, 29% of the mean, in the high enthalpy case. While the laser sheet profile was not measured during the tests, a rough sheet correction was applied to the data by dividing the single shot images by the mean image, which reduces the effect of the (mean) laser sheet intensity profile as well as the laser sheet attenuation. This post-processing reduced the computed fluctuations to 10% of the mean. From this analysis, it is felt that laser sheet inhomogeneity and beam attenuation is causing the majority of the fluctuations in the flow with the flow itself responsible for only 10% of the fluctuations. Still, some of the fluctuations are caused by shot-to-shot variations in the laser sheet spatial intensity profile, which could be removed in future experiments if the laser sheet profile is measured on a shot-to-shot basis. Based on these observations, the uniformity of the flow was determined to be sufficient for the planned mole-fraction-sensitive imaging experiments planned for the facility.

D. NO PLIF Temperature Measurements

We now describe the temperature measurements that were made using NO PLIF. A scan was performed over the $Q_{12}(2)$ and $P_{12}(9)$ lines, which were chosen to minimize absorption (because they are relatively weak lines) and saturation effects, as well as provide differential response to the temperature (because they excite transitions with sufficiently well-separated rotational quantum numbers) for the range that is encountered in our measurements. Figure 8 shows a sample PLIF scan at two different temperatures observed (a) in the nozzle core flow and (b) the shear layer between the core and ambient flow. The observed center wavelengths of the transitions are in agreement with those obtained from LIFBASE software of 2268.29 Å and 2268 Å and 2268.363 Å, respectively.

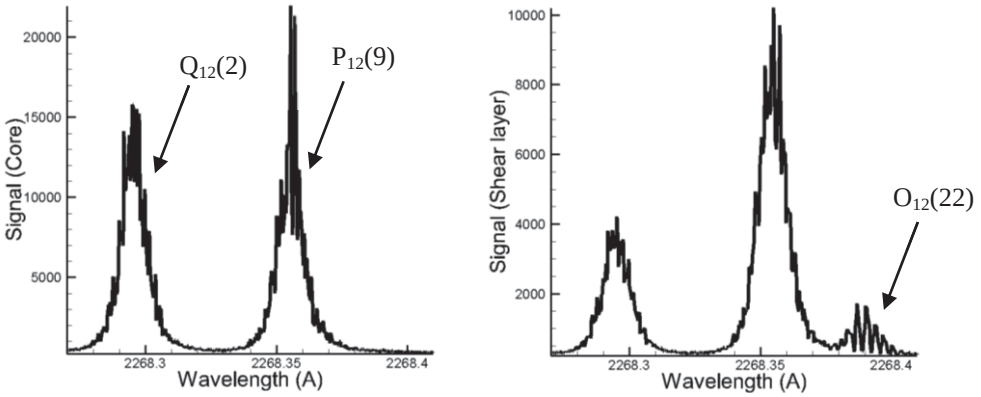

Figure 8. Sample scans in a) the core flow (lower temperature) and b) the shear layer (higher temperature) obtained from different locations in the same image.

Using this scan over these two lines, a temperature map of the nozzle exit plane was created using two-line PLIF thermometry from the ratio of the integrated fluorescence yield at each pixel. This was done using the basic two-line thermometry method developed by Palma et al.[27] and others, as given in Eq. (1).

$$\frac{S_{f1}}{S_{f2}} = \frac{E_1 B_1 (2J_1+1)}{E_2 B_2 (2J_2+1)} \exp\left(\frac{-(F_{J_1} - F_{J_2})}{kT_{rot}}\right) \quad (1)$$

Where

S_f = Integrated line fluorescence
E = Energy of the given electronic state.
B = Einstein B coefficient
J = rotational Quantum number
F_J = Rotational energy of the electronic state
K = Boltzmann's constant

Solving for T_{rot}, the final relation given in Eq. (2) is used:

$$T_{rot} = \frac{(F_{J_2} - F_{J_1})/k}{ln\left(\frac{B_2 E2(2J_2+1)}{B_1 E1(2J_1+1)} \frac{S_{f1}}{S_{f2}}\right)} \quad (2)$$

Assuming equilibrium between rotational and translational degrees of freedom, T_{rot} measures the actual gas temperature. Figure 9 shows the variation of T_{rot} with respect to integrated fluorescence signal ratio $\frac{S_{Q12(2)}}{S_{P12(9)}}$. A monotonic variation of the temperature with the fluorescence ratio can be observed. The fluorescence ratio changes from 0.57 to 2.41 for temperature values between 80K – 200K that are typically observed in the measurements. The

large difference in the fluorescence ratios over the measurement temperatures indicates the potential to obtain high sensitivity in computed temperature.

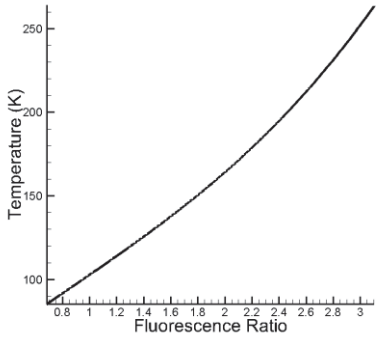

Figure 9. Variation of computed temperature with fluorescence ratio

E. Correspondence between NO PLIF and temperature fields

Figure 10 shows background-subtracted NO PLIF intensity at the peak of the $Q_{12}(2)$ transition (a) and $P_{12}(9)$ transition (b) measured 127 mm downstream of the nozzle exit with a diverging vertical laser sheet configuration for the 440 Btu/lbm (1.02 MJ/kg) enthalpy condition. The similarity in the signal intensities from the two transitions agrees with what would be expected from the nozzle temperature conditions, based on our spectral simulations using LIFBASE. The corresponding signal intensity in the shear layer is considerably different between the two transitions. It can be observed that the $P_{12}(9)$ line image is significantly brighter than the $Q_{12}(2)$ line in this region. This again is expected because of the higher temperatures in the shear layer compared to the core; at high temperatures, the upper J-states have higher population than the lower J-states, which results in higher NO PLIF signal from the $P_{12}(9)$ line. Towards the edges of the image, we observe low signal intensity from NO collected in the test chamber over the course of the experimental run. Even here, there is a perceptible difference in the two images, where the $P_{12}(9)$ line has higher signal counts; this again can be explained due to the higher temperature in the test chamber. Overall, there is a qualitative consistency between the temperature field shown in Fig. 11(a) and the two NO PLIF images. Fluorescence streaks due to laser sheet inhomogeneity are observed, and while these largely cancel out when Eqn. 2 is used to calculate temperature, residual effects of these streaks can be seen in the resulting temperature map when the cancellation of the energy dependence in Eqn. 2 is not perfect owing to slight variations in the laser sheet intensity profile that occurred during the data acquisition.

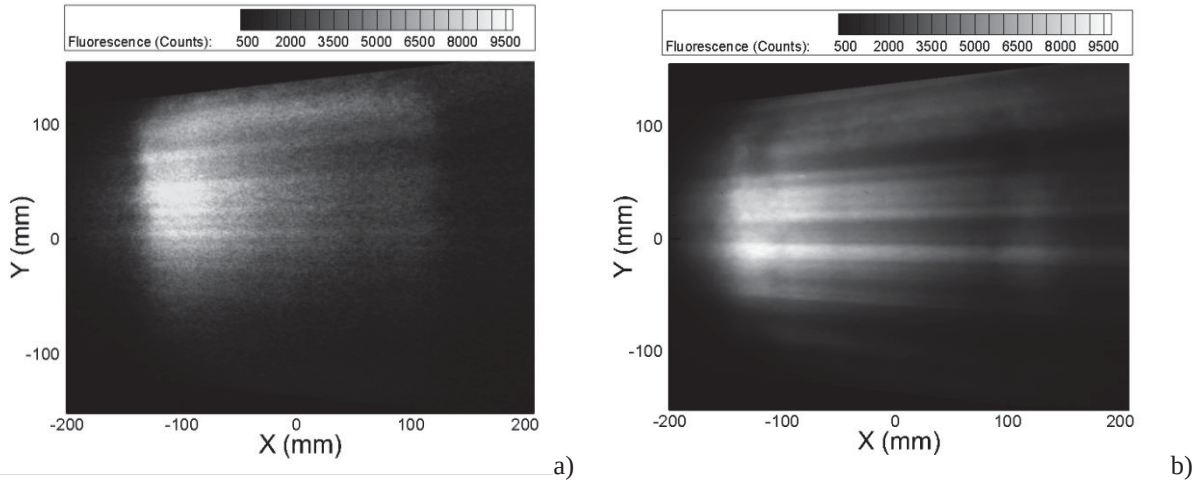

Figure 10. Fluorescence images used for temperature measurement. Run was performed with a diverging laser sheet. Laser is from left to right. Flow is out of the page. Image a) show PLIF obtained by exciting the $Q_{12}(2)$ transition while b) shows the image obtained while exciting the $P_{12}(9)$ transition.

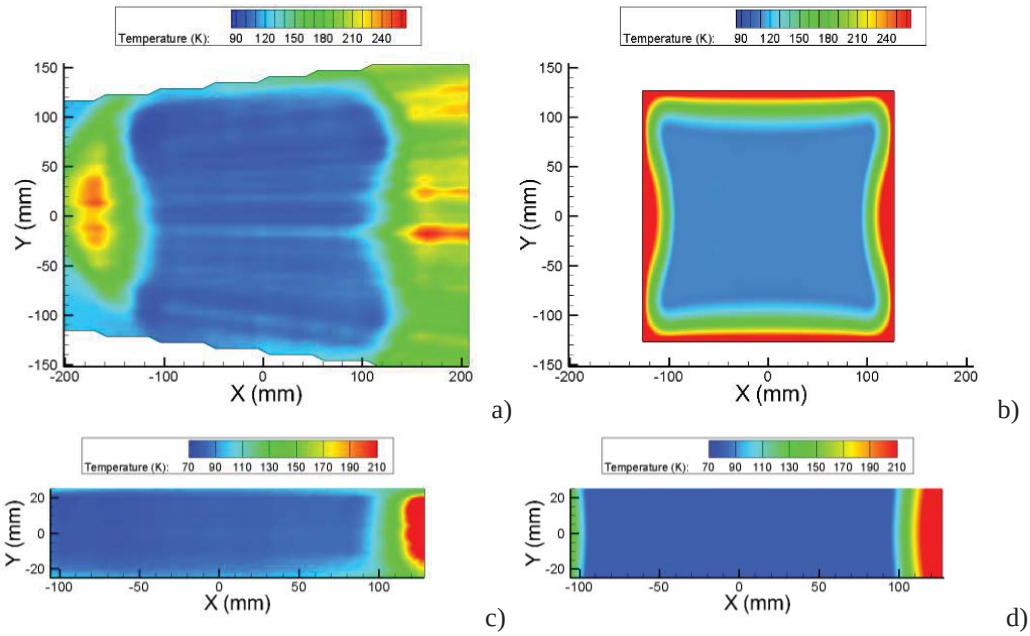

Figure 11. Calculated and CFD temperature plots of nozzle exit flow. Calculated plots were taken 127 mm downstream while CFD is computed for the nozzle exit plane. Figure 11(a) shows a calculated map for high enthalpy (diverging laser sheet) 440 Btu/lbm (1.02 MJ/kg), 11b) shows CFD for high enthalpy, 11c) shows a calculated map for low enthalpy (collimated laser sheet) 335 Btu/lbm (0.779 MJ/kg) and 11(d) shows CFD for low enthalpy.

A major result of these temperature measurements is that the temperature field is relatively uniform across the core flow. The only observed variations in temperature are associated with artifacts from the laser sheet intensity variations. Hypersonic nozzle flows sometimes exhibit nonuniformity in properties (usually pitot pressure) when the nozzles are operated away from the design condition or if the nozzles are damaged or poorly designed (see for example Ref. 28). No such temperature nonuniformities were observed.

A comparison is made between the measured temperature field 127 mm (i.e. 0.5 nozzle diameters) downstream of the nozzle exit and in-house CFD simulations *at the nozzle exit*, shown in Fig. 11. (Physical limitations on the placement of windows and other optical components precluded making measurements much closer than this to the nozzle exit.) Preliminary CFD computations not shown here indicate that the flow from the nozzle exit remains almost collimated downstream of the nozzle exit over a distance of several nozzle diameters, which justifies the comparison at two different streamwise locations within this nearly-collimated region. We observe from Fig. 11 that the experimentally determined temperature field shows some qualitative and quantitative agreement with the CFD simulations. As seen in Fig. 11(a), the mean nozzle temperature determined from the experiments was 102 K, which differs from the computed value of 110 K by 7%. Further, the experimentally determined spatial extent of the nozzle flow, defined as the location where the temperature increases by 10% of its mean value along the y-axis, is approximately 127 mm from the center of the nozzle, which is exactly one half the nozzle exit diameter. This supports the observation that the flow remains fairly collimated in the near-field of the nozzle. It is also interesting to note that both CFD and PLIF fields show a bow shape on the left and right of the core flow (but not on the top and bottom). While the reason for this is not established yet, this is probably due to the differences in the boundary layer growth between the top/bottom walls and side walls, since the nozzle throat is rectangular with subsequent flow expansion occurring only in the y-dimension. The temperature field from the experiments is able to verify this effect. As seen in Fig. 11(c) the mean temperature of the core flow was calculated to be 81.3K This differs from the CFD prediction of 80.6 K by only 1%. We also compare the measured versus computed horizontal temperature profile along the nozzle centerline in Fig. 12. Once again, we observe the agreement in the computational and experimental temperatures to within 8 K in the core for high enthalpy setting and 1 K for the low enthalpy setting. Further, the x-location where the shear layers begin (location where temperature rises from nozzle core temperature) is in very good agreement with CFD. However, the magnitude of the increase in temperature beyond the nozzle core into the shear layer is significantly different. As can be seen in Fig. 11(a,b) The size of the experimentally measured

core flow appears larger in the experiments than the CFD prediction. This is possibly due to the attenuation of the boundary layers as the flow exits the nozzle. Since the CFD was computed at the nozzle exit this would result in a larger effective core flow 127 mm downstream. Overall, we observe quantitative comparison in the temperature values of the core and the qualitative shape of the flow. However, more quantitative comparisons cannot be made without CFD at the experimental plane 127 mm downstream. Also, more quantitative analysis and validation of the PLIF measurements is also needed for a rigorous comparison to be made (to be discussed in more detail below).

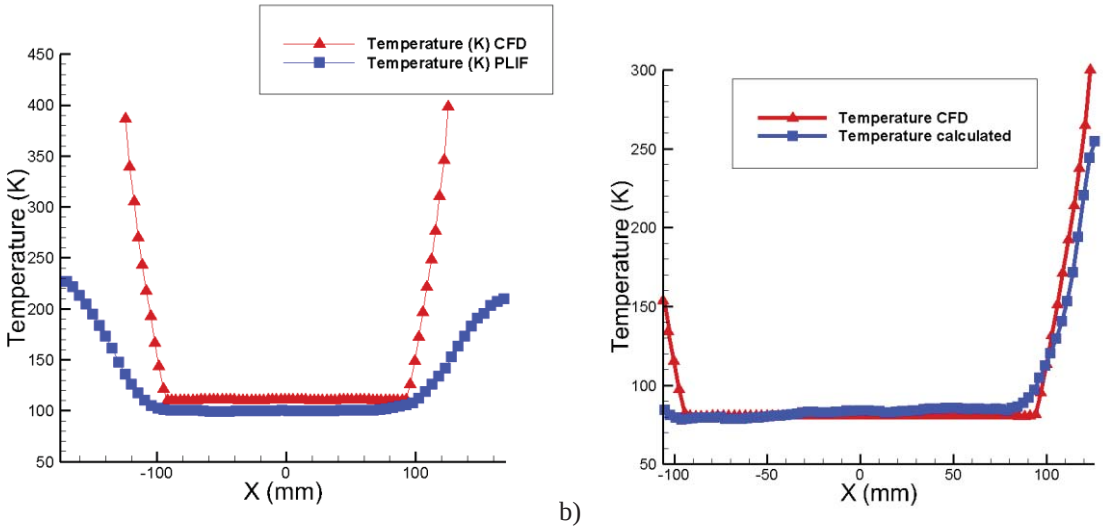

a) b)

Figure 12. Comparison of CFD and PLIF temperature map for both enthalpy settings. (a) high enthalpy 440 Btu/lbm(1.02 MJ/kg); (b) low enthalpy 335 Btu/lbm (0.779MJ/kg.)

F. Uncertainty analysis of measured temperature

For validation purposes, temperature measurements should be made at a known temperature, as was done by O'Byrne et al. in a gas cell.[29] These results could then be compared to the experimental measurements. Since this was not done in the current experiment, the measurements presented herein are not fully quantitative with quantified uncertainty. Nonetheless, a brief investigation of some likely sources of systematic error was performed on the temperature measurements and are reported here. Specifically, we investigated the effects of transition saturation and laser sheet attenuation from absorption on the resulting temperature maps. We also discuss the effect of random signal intensity noise on the measured temperatures.

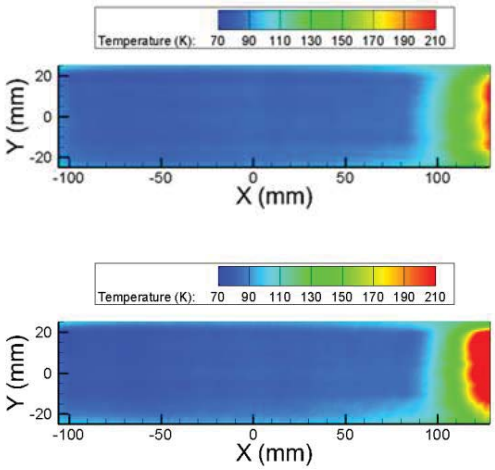

a)

b)

Figure 13. Laser power effects on measured temperature: (a) full power (b) 1/3 of full power.

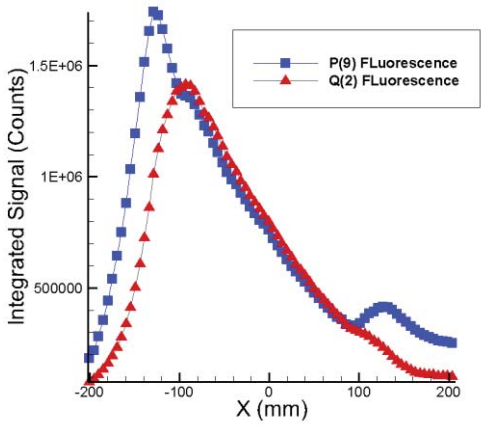

a)

Figure 14. Beam Attenuation of Fluorescing Lines for the high enthalpy setting shown in Fig. 9.

The laser saturation effects are examined by comparing the temperature field from the NO PLIF measurements at identical tunnel operating conditions with the laser operating at different powers. Figure 13 shows two temperature maps constructed at an enthalpy of 335 Btu/lbm (0.779 MJ/kg). Figure 13(a) shows a temperature map with the laser at full power while Fig. 13(b) is at a third of full power. The temperature maps are quantitatively similar with only a 1% difference between the core flow temperatures of 82 K (a), and 81 K (b). Considering that the lower laser power setting will reduce saturation effects, we conclude that saturation effects may contribute to about 1% of uncertainty in the measured temperature at the full power. It is possible that the fluorescence is partially saturated in the raw PLIF images. Yet, if the saturation level is approximately equal for both transitions, then the saturation affect cancels out, having a negligible influence on the measured temperature. Note that the large field-of view temperature measurements shown in this report (such as in Figs. 10 and 11) were obtained with the laser sheet spread out over a four times larger area than in Fig. 13, so the laser intensity in those measurements was typically one fifth of the energy used in Fig. 11(a) and are therefore considered to have negligible influence from saturation.

In addition to saturation effects, the attenuation of the laser sheet by absorption can also lead to temperature errors, for two reasons. First, the differential absorption of the two NO PLIF lines causes changes in the integrated fluorescence ratio, leading to errors in computed temperature. Second, the simultaneous absorption of the two NO PLIF lines can decrease the absolute signal intensities to a level where the inherent camera noise becomes significant. To study the effect of laser absorption, experimental runs were performed with a diverging sheet to minimize the effects of saturation. Figure 11(a) shows a temperature map of the full nozzle flow created with the diverging beam. The uniformity of the temperature across the nozzle core indicates a rather minimal effect of beam attenuation on the temperature. To study the individual absorption of the two NO PLIF lines, Fig. 14 shows the fluorescence intensity of both lines across the nozzle, integrated vertically. It can be seen that, for the core flow, the individual NO PLIF signals of the two lines decrease at almost the same rate, which suggests equal absorption of the individual lines and thus a cancellation in the ratio of the error that would otherwise result. We report the uncertainty in temperature from overall laser absorption effects as the difference in temperature averaged over the left 20% and right 20% of the nozzle core; this value is 1 K over the mean temperature of 102 K.

Finally, we studied the effect of noise in the spectral measurement and its effect on the resulting temperatures. By using LIFBASE's random noise simulation feature, we simulated noise levels in simulated spectra that approximated the levels of noise observed in the experiment, for example in Fig. 9. The noise level corresponded to about 5-10%. Using a set of randomly generated spectra in our analysis software showed that random and systematic errors in the temperature measurements caused by this random noise was about 1-2%.

G. Effect of arc-current on temperature field

The temperature fields presented so far correspond to tunnel run times on the orders of 15-30 seconds where the arc current was kept constant. In the future, NASA plans to operate the tunnel for run times of approximately 5 minutes. In Section 2, we demonstrated that the changing arc current does not change the NO PLIF signal intensity. In this section, we characterize the influence of the arc current on the measured temperature field. Figure 15 shows temperature maps for arc-current settings of (a) 1600 A, (b) 1850 A, and (c) 2200 A, respectively (gas flow rates were varied to maintain constant enthalpy). The corresponding line plot of the nozzle centerline temperature for the

three runs is presented in Fig. 15(d). The high temperature regions to the left and right of the core flow are believed to be caused by the turbulent boundary layer exiting the nozzle. Between the three runs, the temperature changed over an 8 K range (102 K (a), 109 K (b), 104 K (c)) in the nozzle core. This non-monotonic change in temperature, however, corresponds to slight differences in the actual enthalpy of each run. Hence, it appears that the temperature of the tunnel core flow and the surrounding flow field are not appreciably affected by the changing current conditions.

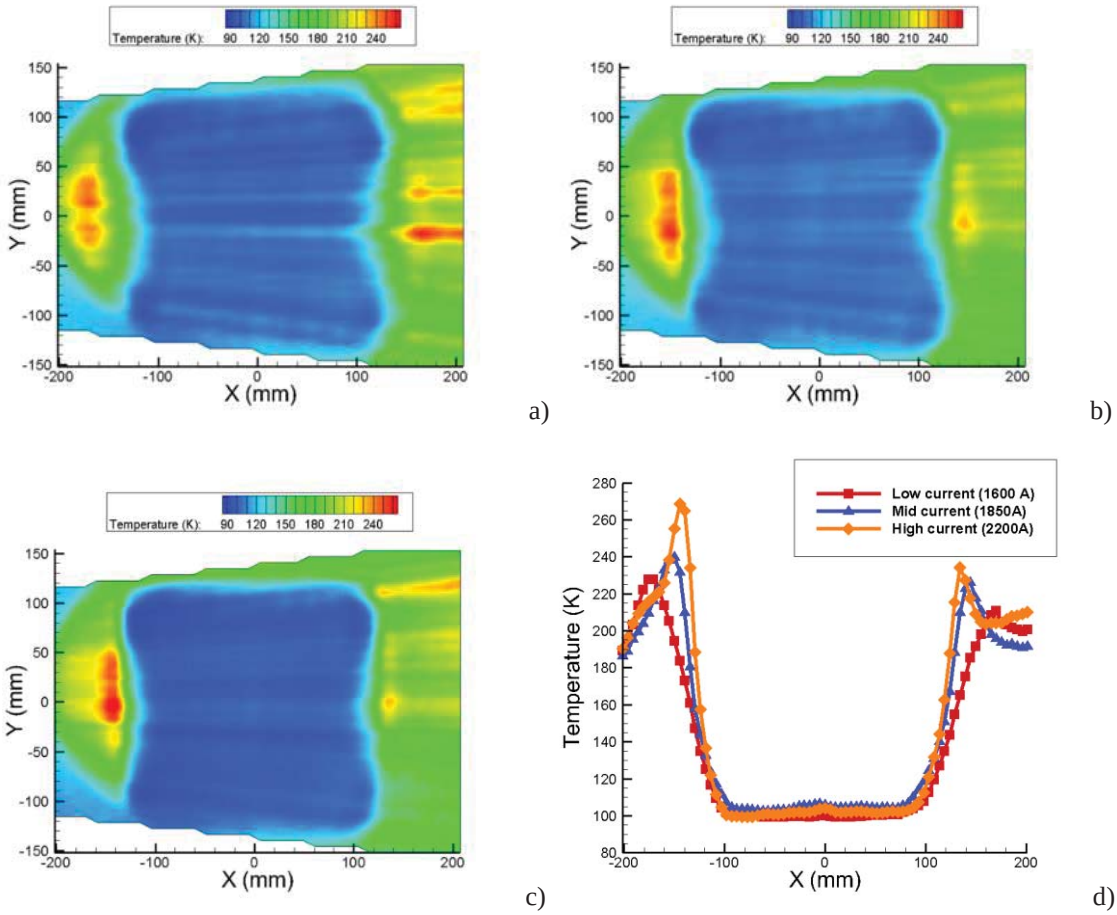

Figure 15. Temperature maps of full nozzle exit showing variation of temperature with current. (a) 1600A; (b) 1850A; (c) 2200A.

H. Effect of enthalpy on temperature field

This section examines the effect of stagnation enthalpy setting on the corresponding temperature field. We are interested in determining the magnitude of temperature change in the nozzle core corresponding to changes in enthalpy and the overall qualitative differences in the flowfield that may be caused by the stagnation-enthalpy setting. Figure 16 shows temperature maps for the high and low enthalpy settings. The nozzle core temperature of the low and high enthalpy settings respectively are 81 K and 101 K, a 20 percent difference. The corresponding values from CFD simulations are 80.5 K and 110 K respectively (about a 30% difference). The measured temperature increase is roughly the same as the enthalpy increase (20% vs. 24%) and even closer to the measured change in stagnation temperature of 23%, which is expected with a fixed Mach number nozzle. A qualitative comparison is also made between the two temperature fields to discern the changes in the flowfield between the two settings. Overall there is a qualitative similarity between the two settings in terms of the uniformity of the temperature field. Also from Fig. 16(c), it can be observed that the location of the shear layer is unchanged between enthalpy settings.

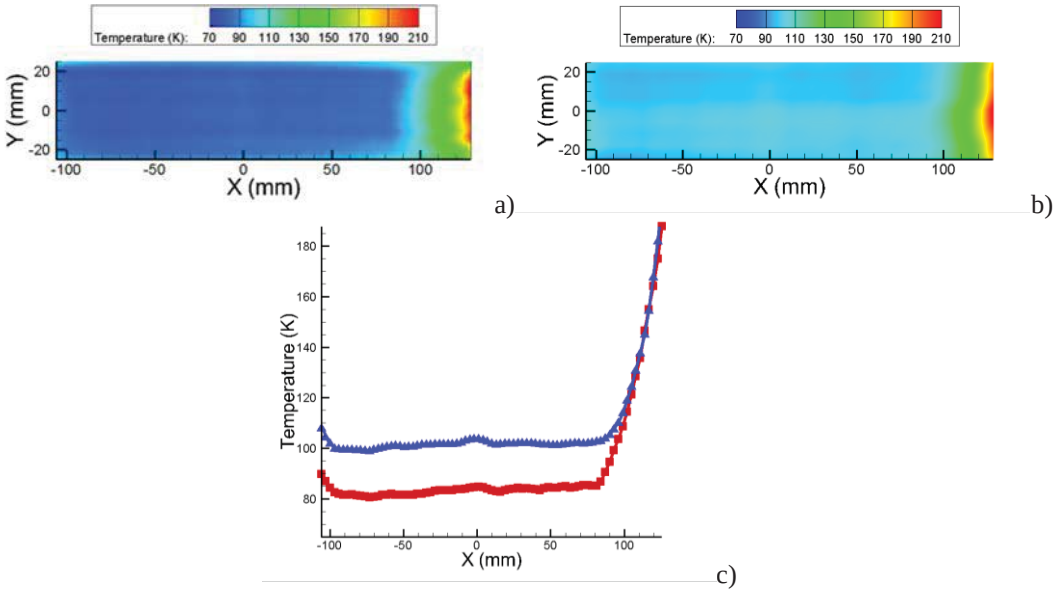

Figure 16. Temperature maps of plane 127 mm downstream of Nozzle Exit showing variation of temperature with enthalpy. Figure (a) shows low enthalpy (335 Btu/lbm, 0.779 MJ/kg) while shows (b) high enthalpy (440 Btu/lbm, 1.02 MJ/kg). Figure (c) shows a plot of two slices across the flow obtained at y=0.

I. Visualization of expansion and compression waves

The temperature maps can also be used to identify wave features in the flow field at different operating conditions. It is believed that the longer than regular run times will cause the pressure to rise in the test section and lead to the development of shock waves corresponding to over-expanded operation. The ability to visualize the wave structures would also be beneficial for future experiments, especially if it can be done in concert with the existing system. Figure 17 shows temperature field at different times during the run with pressure ratio of nozzle exit pressure to test section pressure of (a) 0.948 and (b) 1.89, keeping the stagnation enthalpy constant. The difference in the measured temperature is due to the increased beam attenuation caused by the increased chamber pressure in Fig. 17(b), which causes a differential absorption of the two NO PLIF transitions $Q_{12}(2)$ and $P_{12}(9)$ used for temperature field determination. This causes the later part of the run shown in Fig. 17(b) to appear cooler. Figure 17(c) shows the temperature gradient plot corresponding to Fig. 17(b). Comparing Fig, 17(c) and 17(b) shows the presence of two temperature gradients along the X-axis, a sharp one within the core flow from X = -50 mm to -65 mm and a spatially broad one which overlaps with the shear layer location from -70 mm to -90 mm. The sharp temperature gradient suggests the presence of an oblique shock wave. To ascertain whether it is indeed an oblique shock wave, we measured and compared the shock angle derived from the temperature field. The angle measured from Fig. 17(c) was 12.9 degrees. The angle matches closely the expected values from NACA TN D-2221[30] for a

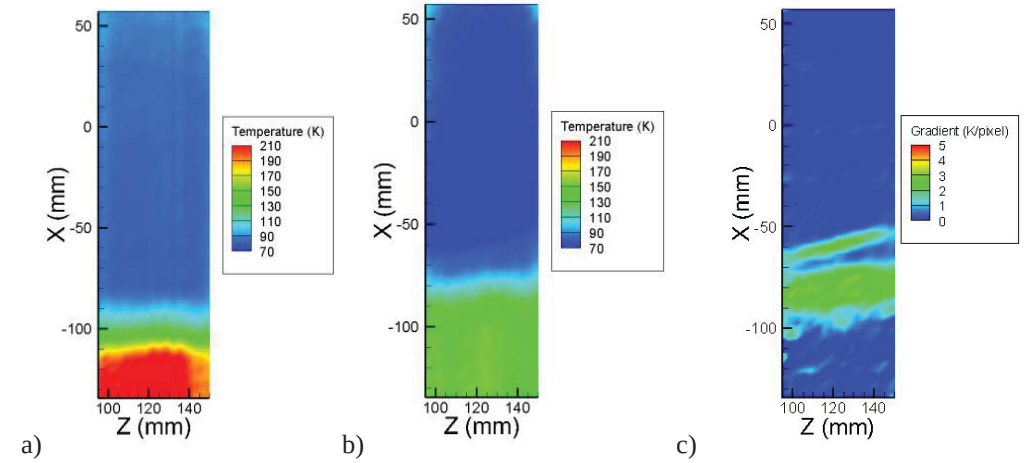

Figure 17. Temperature maps showing shock wave propagation (Z is normal to nozzle exit plane). Figure (a) is early in the run, (b) is a later point in the run. Figure (c) shows the temperature gradient map corresponding to (b).

Mach 6.4 flow, which predicts an 11.7 degree shock angle at a the measured pressure ratio of 1.89. In addition, the streamline deflection downstream of the shock wave was determined to have an angle of 4 degrees, based on the orientation of the shear layer, which in turn was obtained from the temperature gradient iso-contour. This computed angle of 4-degrees once again matches quite well with the theoretical values of 4 degrees. The corresponding temperature gradient map for Fig. 17(a) (not shown) indicates that the temperature gradients only occur in the shear layer. This suggests that Fig. 17(a) appears to be an almost perfectly expanded flow. The CFD results corroborate this observation of a perfect expansion at the back pressure conditions corresponding to Fig. 17(a).

IV. Conclusions

These experiments have demonstrated that NO exists in sufficient quantity to produce high quality NO PLIF images in the NASA Langley Arc Heated Scramjet Test Facility configured with a Mach 6 nozzle operating at a lower total enthalpy than used previously. The quality of the resulting images was assessed. The shot to shot PLIF signal variations were determined to be about 20% of the mean while within individual images, the signal variation was observed to be closer to 30% although within the images, much of the signal variation was caused by variations in laser energy caused by the intensity profile of the laser as well as the attenuation of the laser sheet as it is absorbed while passing through the flow. Roughly compensating for these two laser-based artifacts in image processing suggests that the underlying signal intensity variation caused by NO concentration variations is about 10% of the mean. No significant difference in PLIF signal uniformity was observed between the lower and higher enthalpy cases tested. Such uniformity has been determined to be sufficient for planned fuel/air mixing experiments which will use NO PLIF to qualitatively monitor and compare the performance of different fuel injectors. The PLIF signal increased with flow enthalpy mainly because of increasing NO concentration. On the other hand, as the facility arc current varied, holding the enthalpy constant (by varying the gas flowrates), the PLIF signal remained constant, indicating that the NO concentration was held constant, as desired. Temperature measurements have been performed and qualitatively match the expected trends predicted by CFD. Qualitative temperature maps also allow the mapping of wave features. It is believed that, in future experiments, temperature measurements may be able to produce quantitative results if errors caused by absorption and saturation of the lines are carefully controlled, but a more detailed uncertainty analysis and comparison with "known" references is necessary before measurements are deemed to be fully quantitative. For quantitative measurements, particular attention will need to be paid to the absorption between the laser's entry window and the core flow. This problem could be mitigated in part by building a window insert (a light pipe) to allow the laser sheet to get much closer to the flow before passing through the window into the flow to minimize absorption. Furthermore, for mole fraction measurements PLIF measurements may have to be limited the initial part (first minute) of the run, before the pressure builds up in the test section to avoid absorption which attenuate the laser sheet, decreasing the fluorescence and possibly causing systematic errors or misinterpretation of the results.

References

[1] Guy, R. W., Rogers, C. R., Puster, R. L., Rock, K. E., Diskin, G. S., "The NASA Langley Scramjet Test Complex," AIAA Paper 96-3243, 32nd AIAA/ASME/SAE/ASEE Joint Propulsion Conference (1996).

[2] Palma, P. C., Danehy, P. M., Houwing, A. F. P., "Fluorescence Imaging of Rotational and Vibrational Temperature in a Shock Tunnel Nozzle Flow," AIAA Journal, Vol. 41, No. 9, Sept. p. 1722-1732 (2003).

[3] McMillin, B. K., Seitzman, J. M., Hanson, R. K., "Comparison of NO and OH PLIF Temperature Measurements in a Scramjet Model Flowfield," paper AIAA-93-2035 at 29th AIAA/SAE/ASME/ASEE Joint Propulsion Conf., Monterey, CA, June 1993; also AIAA J. 32 1945-1952 (1994).

[4] McDaniel, J. C., Hiller, B., Hanson, R. K., "Simultaneous multi point velocity measurements using laser induced iodine fluorescence," Optics Letters, Vol. 8, Issue 1, pp. 51-53 (1983) http://dx.doi.org/10.1364/OL.8.000051

[5] Hsu, A.G., Narayanaswamy, V., Clemens, N.T., Frank, J.H., "Mixture Fraction Imaging in turbulent non-premixed flames with two-photon LIF of krypton," Proc Combust Inst, 33 (2010), pp. 759–766.

[6] Narayanaswamy, V., Burns, R., and Clemens, N. T., "Kr-PLIF for scalar imaging in supersonic flows," Optics Letters, Vol. 36, Issue 21, pp. 4185-4187 (2011) http://dx.doi.org/10.1364/OL.36.004185 http://dx.doi.org/10.1364/OL.36.004185

[7] Koch, U., Guålhan, K ., Esser, B., Grisch, F., and Bouchardy, P., "Rotational and Vibrational Temperature and Density Measurements by Planar Laser Induced NO-Fluorescence Spectroscopy in a Nonequilibrium High Enthalpy Flow," AGARD Fluid Dynamics Panel Symposium, Advanced A ¦qn¹Ôs. t¥«´ Measurement Technology, CP-601, AGARD, 1 997 , Paper 15 12

[8] Gulhan, A., "Coherent Anti-Stokes Raman Scattering Measurements and Computational Modeling of Nonequilibrium Flow," AIAA Journal, Vol. 38, No. 9, 2000, pp. 166 9 -16 7 5.

[9] Palma, P. C., Mallinson, S. G., O'Byrne, S. B., Danehy, P. M., and Hillier, R., "Temperature measurements in a hypersonic boundary layer using planar laser-induced fluorescence," AIAA Journal, Vol. 38, No. 9, p. 1769-1772 (2000).

[10] Fox, J. S., O'Byrne, S., Houwing, A. F. P., Papinniemi, A., Danehy, P. M., Mudford, N. R., "Fluorescence Visualization of Hypersonic Flow Establishment over a Blunt Fin," AIAA Journal, v. 39(7), p. 1329-1337 (2001).

[11] Ivey, C. B., Danehy, P. M., Bathel, B. F., Dyakonov, A. A., Inman, J. A., and Jones, S. B., "Comparison of PLIF and CFD Results for the Orion CEV RCS Jets," 49th AIAA Aerospace Sciences Meeting, Paper AIAA-2011-713, Fluid Dynamics TC, Orlando Florida, January 2011.

[12] Inman, J. A., Danehy, P. M., Alderfer, D. W., Buck, G. M., and McCrea, A., "Planar Fluorescence Imaging and Three Dimensional Reconstructions of Capsule Reaction-Control-System Jets," AIAA Journal Vol. 47, No. 4, April (2009).

[13] Fox, J. S., Houwing, A. F. P., Danehy, P. M., Gaston, M. J., Mudford, N. R., and Gai, S. L., "Mole-Fraction-Sensitive Imaging of Hypermixing Shear Layers," *Journal of Propulsion and Power*, 17, 2 (2001), 284 - 292.

[14] Guy, R. W., Torrence, M. G., Sabol, A.P., and Mueller, J.N., "Operating Characteristics of the Langley Mach 7 Scramjet Test Facility," *NASA TM-81929* (1981).

[15] Thomas, S. R. and Guy, R.W., "Expanded Operational Capabilities of the Langley Mach 7 Scramjet Test Facility," *NASA TP-2186* (1983).

[16] Howard, R. P., Dietz, K. L., McGregor, W. K., and Limbaugh, C. C. Nonintrusive Nitric Oxide Density Measurements in the NASA Langley Arc-Heated Scramjet Test Facility. *AEDC-TR-90-26* (1991).

[17] MacDermott, W. N., Horn, D. D., and Fisher, C. J.. "Flow Contamination and Flow Quality in Arc Heaters Used for Hypersonic Testing" *AIAA Paper 92-4028, AIAA 17th Aerospace Ground Testing Conference, Nashville, TN* (1992).

[18] Cabell, K. F. and Rock, K.E.. "A Finite Rate Chemical Analysis of Nitric Oxide Flow Contamination Effects on Scramjet Performance," *NASA TP-212159* (2003).

[19] Personal Communication, R. Baurle, NASA Langley Research Center, Hampton VA.

[20] VULCAN, http://vulcan-cfd.larc.nasa.gov/, 2012.

[21] van Leer, B., "Towards the ultimate conservative difference scheme." v. a second-order sequel to Godunov's method, J. Comput. Phys., 32(1):101–136, 1979.

[22] Edwards, J.R., "A low-diffusion flux-splitting scheme for Navier-Stokes calculations," Comput. Fluids., 26(6):635–659, 1997.

[23] McBride, B.J., Gordon, S., and Reno, M.A., "Thermodynamic data for fifty reference elements," NASA Technical Paper 3287/REV1, NASA, Cleveland, OH, 2001.

[24] Pulliam, T.H. and Chaussee, D.S., "A diagonal form of an implicit approximate-factorization algorithm," J. Comput. Phys., 39(2):347–363, 1981.

[25] Menter, F.R., "Two-equation eddy-viscosity turbulence models for engineering applications," AIAA Journal, 32, No. 8:1598–1605, 1994.

[26] Wilcox, D.C., "Turbulence Modeling for CFD," DCW Industries, Inc., La Canada, CA, 2000.

[27] Palma, P. C., "Laser-Induced Fluorescence Imaging in Free-Piston Shock Tunnels," Ph.D. Dissertation, Physics Dept., Australian National Univ., Canberra, Australian Capital Territory, Australia, 1999, URL: http://www.anu.edu.au/Physics/aldir/publications/Palma PhD 1999.pdf.

[28] MacLean, M.; Candler, G.; and Holden, M. "Numerical Evaluation of Flow Conditions in the LENS Reflected Shock-Tunnel Facilities". AIAA Paper 2005-0903. 43RD Aerospace Sciences Meeting & Exhibit. Reno, NV: 10-14 January 2005.

[29] O'Byrne, S., Danehy, P. M., Houwing, A. F. P., "Investigation of hypersonic nozzle flow uniformity using NO fluorescence," Shock Waves Journal, May, Pages 1 - 7, DOI 10.1007/s00193-006-0013-6, URL http://dx.doi.org/10.1007/s00193-006-0013-6 (2006).

[30] Dennard, J. S., Spencer, P. B., "Ideal-gas tables for oblique-shock flow parameters in air at Mach numbers from 1.05 to 12.0," *NASA TN D-2221 (1964)*